Supplemental Material for: Thermally superactive artificial kagome spin ice structures obtained with the interfacial Dzyaloshinskii-Moriya interaction

Kevin Hofhuis,[1,2,*] Aleš Hrabec,[1,2,3] Hanu Arava,[1,2] Naëmi Leo,[1,2] Yen-Lin Huang,[4] Rajesh V. Chopdekar,[5] Sergii Parchenko,[1,2,6] Armin Kleibert,[6] Sabri Koraltan,[7] Claas Abert,[7] Christoph Vogler,[7] Dieter Suess,[7] Peter Michael Derlet,[1,8] and Laura Jane Heyderman[1,2,†]

[1] *Laboratory for Mesoscopic Systems, Department of Materials, ETH Zurich, 8093 Zurich, Switzerland*
[2] *Laboratory for Multiscale Materials Experiments, Paul Scherrer Institute, 5232 Villigen PSI, Switzerland*
[3] *Laboratory for Magnetism and Interface Physics, Department of Materials, ETH Zurich, 8093 Zurich, Switzerland*
[4] *Department of Materials Science and Engineering, University of California, Berkeley, California 94720, USA*
[5] *Advanced Light Source, Lawrence Berkeley National Laboratory (LBNL), 1 Cyclotron Road, Berkeley, CA 94720, USA*
[6] *Swiss Light Source (SLS), Paul Scherrer Institute, 5232 Villigen PSI, Switzerland*
[7] *Christian Doppler Laboratory, Advanced Magnetic Sensing and Materials, University of Vienna, Waehringer Strasse 17, 1090, Vienna, Austria*
[8] *Condensed Matter Theory Group, Paul Scherrer Institute, 5232 Villigen PSI, Switzerland*

(Dated: October 15, 2020)

Thermally active artificial spin ice provides a model system for geometric frustration in which the nanomagnetic moments take on the role of Ising spins that can be imaged in real-space and real-time. For the kagome spin ice, two long-range ordered phases have been predicted [1, 2], but these have not been experimentally verified. In order to observe these equilibrium phases, it is necessary to lower the reduced blocking temperature $T_{\mathrm{B}}/J_{\mathrm{NN}}$ to below the critical temperatures for the phase transitions. For artificial kagome spin ice, the critical temperatures are $T_{\mathrm{crit}}^{\mathrm{charge}} = 0.35 J_{\mathrm{NN}}$ and $T_{\mathrm{crit}}^{\mathrm{spin}} \approx 0.12 J_{\mathrm{NN}}$.

I ESTIMATION OF NANOMAGNET INTERACTION STRENGTH

In order to derive the dependence of both T_{B} and J_{NN} on the geometrical and material parameters, we focus on the dipolar interactions between nanomagnets, which are given by the dipolar pre-factor

$$J_{\mathrm{NN}} = \frac{\mu_0 m^2}{4\pi a^3} \propto \frac{m^2}{a^3}\,. \tag{1}$$

Here μ_0 is the vacuum permeability, a is the lattice constant between nearest-neighbours, and m is the magnitude of the magnetic moment given by

$$m = M_{\mathrm{sat}} V, \tag{2}$$

where M_{sat} is the magnetisation at saturation and the volume V of a stadium-shaped nanomagnet is given by

$$V = \left(L - \frac{\pi - 4}{4} W\right) W h \propto L^2 h\,, \tag{3}$$

where L is the nanomagnet length, $W = L/3$ is the nanomagnet width with a fixed aspect ratio, and h is the thickness of the nanomagnets that are spaced apart with the lattice constant

$$a \approx L + g \approx L\,, \tag{4}$$

where g is the gap ($g = 20\,\mathrm{nm} \ll L$), which is the smallest separation between neighbouring nanomagnets (see Fig. 1 of the main text). Hence the dipolar interactions can be simplified to

$$J_{\mathrm{NN}} \propto M_{\mathrm{sat}}^2 L h^2\,. \tag{5}$$

II DERIVATION OF BLOCKING TEMPERATURE REDUCTION BY INTERFACIAL DMI

The energy barrier E_{B} that determines the blocking temperature T_{B} depends, to a first approximation, on the shape and volume of the nanomagnet K_{xy}, as well as the DMI anisotropy K_{DMI} resulting from the interfacial coupling with the heavy-metal layer. Following the same arguments laid out by Cubukcu *et al.* [3], the effective anisotropy due to the interfacial DMI of a simple rectangle is given by

$$K_{\mathrm{DMI}} \approx \frac{D_s^2}{h^2 \sqrt{A_{\mathrm{ex}} K_{xz}}} \frac{L - W}{LW}\,, \tag{6}$$

where A_{ex} is the exchange stiffness constant, K_{xz} is the out-of-plane shape anisotropy, and D_{s} is the surface DMI strength that follows from the thickness-dependent effective DMI strength D [4] given by

$$D = \frac{D_{\mathrm{s}}}{h}\,. \tag{7}$$

The blocking temperature is then proportional to

$$T_{\mathrm{B}} = \frac{E_{\mathrm{B}}}{k_{\mathrm{B}} \ln \frac{\tau_m}{\tau_0}} \propto (K_{xy} - K_{\mathrm{DMI}})\, V\,, \tag{8}$$

where k_{B} is the Boltzmann constant, τ_m is the characteristic measurement time, and τ_0 the inverse attempt frequency [5]. The in-plane shape anisotropy K_{xy} is given

* khofhuis@gmail.com
† laura.heyderman@psi.ch

by

$$K_{xy} = \frac{1}{2}\mu_0 M_{\rm sat}^2 \left(\mathcal{N}_x - \mathcal{N}_y\right) , \tag{9}$$

and the out-of-plane shape anisotropy is given by

$$K_{xz} = \frac{1}{2}\mu_0 M_{\rm sat}^2 \left(\mathcal{N}_x - \mathcal{N}_z\right) - K_u , \tag{10}$$

where $\mathcal{N}_i$ are the demagnetisation factors along the three axes ($i = [x, y, z]$) and K_u is the uniaxial anisotropy (assumed to be zero for $Ni_{80}Fe_{20}$). The blocking temperature is then given by

$$T_{\rm B} \propto \left(K_{xy} - \frac{2D_s^2}{\sqrt{A_{\rm ex}K_{xz}}} \frac{1}{Lh^2} \right) L^2 h , \tag{11}$$

and the reduced blocking temperature is given by

$$\frac{T_{\rm B}}{J_{\rm NN}} \propto \left(K_{xy} \frac{L}{h} - \frac{2D_s^2}{\sqrt{A_{\rm ex}K_{xz}}} \frac{1}{h^3} \right) . \tag{12}$$

The reduced blocking temperature Eqn. (12) is smaller for smaller lateral nanomagnet lengths L, which should result in better magnetic ordering. Furthermore, thinner nanomagnets would result in a lowering of the reduced blocking temperature due to the increased effective DMI strength.

III MINIMUM ENERGY PATH AND ENERGY BARRIER SIMULATION

In order to calculate the energy barriers between the two easy axis magnetisation states, we use the simplified and improved string method [6–8]. The string method computes the minimum energy transition path by employing an iterative approach so that the initial path evolves iteratively towards the minimum energy path (MEP). The MEP represents the energetically most favourable way to switch the magnetisation between the new, relaxed initial state and the new, relaxed final state.

The string method is implemented in magnum.fe, a micromagnetic simulation code based on the finite element method [9]. To create the geometry of the five nanomagnets and generate the finite element meshes, we use GMSH, an open-source 3D finite element grid generator [10]. For our calculations, we consider one central nanomagnet, with the easy axis along the x-direction, surrounded by its four nearest-neighbours (NN), see Supplementary Movies [11].

In the simulations, we used the magnetic material parameters of bulk $Ni_{80}Fe_{20}$, with a saturation magnetisation $M_{\rm sat} = 790\,\mathrm{kA/m}$ and exchange stiffness constant $A_{\rm ex} = 13\,\mathrm{pJ/m}$. To determine the effect of the interfacial Dzyaloshinskii-Moriya interaction (DMI), we vary the DMI strength between $D = 0.0\,\mathrm{mJ/m^2}$ and $D = 2.0\,\mathrm{mJ/m^2}$.

As an initial step, the reversal of the central nanomagnet is assumed to be a coherent rotation from a uniform initial state with $\hat{\boldsymbol{m}}_{\rm ini} = (-1, 0, 0)$ to a uniform final state with $\hat{\boldsymbol{m}}_{\rm end} = (1, 0, 0)$. Here, $\hat{\boldsymbol{m}}$ denotes the unit-vector-field representation of the magnetisation configuration. This initial path is divided into 21 equidistant states with respect to the energy-weighted arc length of the rotation.

We consider the total energy of the system to be

$$E^{\rm tot} = E^{\rm dem} + E^{\rm ex} + E^{\rm DMI} , \tag{13}$$

where $E^{\rm dem}$ is the demagnetizing energy, $E^{\rm ex}$ is the ferromagnetic exchange energy, and $E^{\rm DMI}$ is the antisymmetric exchange energy. The demagnetizing energy is given by

$$E^{\rm dem} = -\frac{\mu_0 M_{\rm sat}}{2} \int_{\Omega_{\rm m}} \boldsymbol{m} \cdot \boldsymbol{H}^{\rm dem} \mathrm{d}\boldsymbol{x} , \tag{14}$$

with $\Omega_{\rm m}$ corresponding to the region containing magnetic material $\boldsymbol{m}$ i.e. the five magnetic nanomagnets, and the demagnetisation field $\boldsymbol{H}^{\rm dem}$ given by

$$\boldsymbol{H}^{\rm dem}(\boldsymbol{x}) = -\frac{M_{\rm sat}}{4\pi} \int_{\Omega_{\rm m}} \nabla\nabla' \frac{1}{|\boldsymbol{x} - \boldsymbol{x'}|} \boldsymbol{m}(\boldsymbol{x'}) \mathrm{d}\boldsymbol{x'} . \tag{15}$$

The ferromagnetic exchange energy is given by

$$E^{\rm ex} = \int_{\Omega_{\rm m}} A_{\rm ex} (\nabla \boldsymbol{m})^2 \mathrm{d}\boldsymbol{x}, \tag{16}$$

and the antisymmetric exchange energy due to the interfacial DMI is given by

$$E^{\rm DMI} = \int_{\Omega_{\rm m}} D[\boldsymbol{m} \cdot \nabla(\boldsymbol{e}_{\rm d} \cdot \boldsymbol{m}) - (\nabla \cdot \boldsymbol{m})(\boldsymbol{e}_{\rm d} \cdot \boldsymbol{m})] \mathrm{d}\boldsymbol{x} , \tag{17}$$

with $\boldsymbol{e}_{\rm d}$ being the surface normal to the ferromagnetic-heavy metal interface. The energy barrier $E_{\rm B}$ can be computed using

$$E_{\rm B} = E^{\rm saddle} - E^{\rm ini} , \tag{18}$$

where $E^{\rm saddle}$ is the energy corresponding to the saddle point of the MEP (State 10) and $E^{\rm ini}$ is the energy corresponding to the initial magnetisation (State 0).

The full animation of the magnetisation reversals with and without the interfacial DMI are provided in the Supplementary Movies [11], where the colour scale represents the out-of-plane magnetisation component $\mathbf{m}_z$. It can be seen that, with the interfacial DMI, the reversal is more coherent as a result of the additional short-axis anisotropy.

IV EFFECT OF ROUGHNESS

To address the influence of lithographic edge roughness on the blocking temperature, we performed the energy barrier simulations for nanomagnets with DMI as shown in Suppl. Fig. 1. Scanning electron microscopy (SEM) images were used to define the geometry. Comparing nanomagnets with and without edge roughness, while keeping the magnetic moment constant, we find that there is a significant increase in the energy barrier by

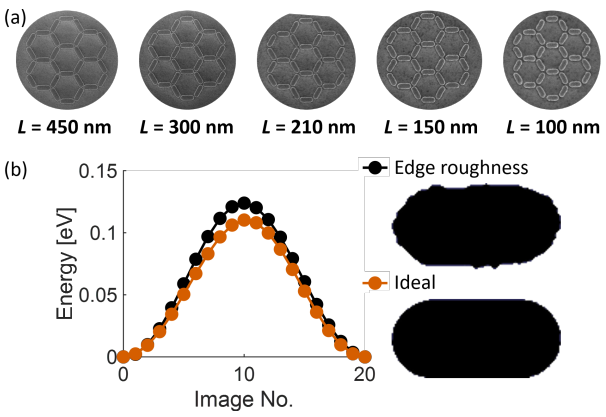

Suppl. Fig. 1. (a) Experimental scanning electron microscopy (SEM) image series of seven-ring artificial kagome spin ice structures with $L = 450\,\text{nm}$, 300 nm, 210 nm, 150 nm and 100 nm. (b) Energy barrier simulation of a nanomagnet of length $L = 100\,\text{nm}$ and aspect ratio $L/W = 3$ with and without edge roughness. To include the edge roughness, the shape is taken from an SEM image of a nanomagnet of length $L = 100\,\text{nm}$ (top image). This is compared to the ideal nanomagnet (bottom image) with only small edge roughness resulting from the meshing (bottom image). In the energy barrier simulations, the total volume, and therefore the magnetic moment, of both the nanomagnet with edge roughness and the ideal nanomagnet is the same.

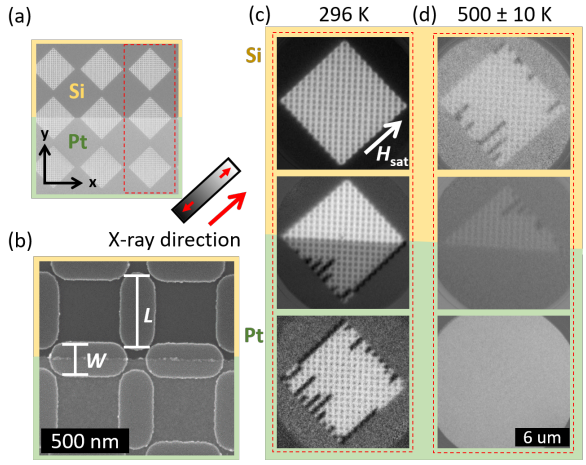

Suppl. Fig. 2. (a) Scanning electron microscope (SEM) image of wedge sample of variable $Ni_{80}Fe_{20}$ thickness along the x-axis of the sample and (b) a zoom in of nanomagnets with their lateral dimensions L and $W = L/3$ indicated. The Si and Pt surface are indicated and can be seen in de zoom in (b) where the higher contrast surface is coming from the Pt. The red box in (a) indicates the thermally active $Ni_{80}Fe_{20}$ of thickness 4.2 nm artificial square ice on a 5 nm Pt layer at room temperature (RT) imaged with time dependent X-PEEM. In X-PEEM, nanomagnets with moments pointing towards the x-ray propagation direction, see red arrow in (a), appear bright, while moments opposing the incoming x-rays appear dark. On Si, the identically prepared array is still in a remanent magnetization state (all white) after saturating with an in-situ field applied in the direction of the x-rays. (c) On heating to 500 K, the nanomagnets on Si become thermally active on the same timescale as those on Pt at 296 K. Simultaneously, the magnetic contrast of $Ni_{80}Fe_{20}$ on Pt disappears at 500 K due to the high switching rate of the nanomagnets, resulting in an averaged grey contrast.

13.6 meV or 10 % on introducing edge roughness. This corresponds to a factor of 24 in the reorientation frequency at 50 K. This is due to the fact that, with the interfacial DMI, coherent rotation is favoured and the added edge roughness gives rise to a non-uniform state that leads to an increase in the energy barrier.

V DIRECT VISUALIZATION OF THE REDUCTION OF T_B DUE TO INTERFACIAL DMI IN X-PEEM

In order to experimentally verify the origin of the reduced blocking temperature, we first measured the saturation magnetization of nanomagnets with and without the interface to the heavy-metal Pt. For this, we performed SQUID-VSM measurements and determined that identically grown $Ni_{80}Fe_{20}$ nanomagnets (with dimensions $L = 450\,\text{nm}$, $W = 150\,\text{nm}$, and $h = 4.2\,\text{nm}$) on 5 nm Pt and on a Si substrate have the same saturation magnetization M_{sat} of 360 kA/m.

In order to experimentally verify that Pt induces an interfacial DMI, we fabricated a Pt strip on a Si substrate. We then patterned arrays of $Ni_{80}Fe_{20}$ nanomagnets, both on the Pt strip and the neighbouring Si substrate, depositing a film wedge to obtain nanomagnet arrays with different thickness. We measured the blocking temperatures using time-dependent X-PEEM [12], and the nanomagnet thickness is varied along the x-direction of the sample, see Suppl. Fig. 2(a), ensuring a blocking temperature T_B within the accessible temperature range of the X-PEEM. The overall size of each individual array is 22 by 22 nanomagnets, occupying an area of $10\,\mu\text{m} \times 10\,\mu\text{m}$. A control array was fabricated on top of both the Si and Pt interface in order to observe the effect of Pt inside a single circular field-of-view with a diameter of 15 µm, see Suppl. Fig. 2.

Magnetic imaging was performed at the SIM beamline PEEM endstation at the Swiss Light Source, employing x-ray magnetic circular dichroism (XMCD) at the Fe L_3 edge [13]. XMCD contrast images are obtained by pixel-wise division of images recorded with right and left circularly polarized x-rays. The resulting XMCD contrast gives a direct measure of the projection of the magnetic moments onto the x-ray propagation vector. Moments pointing towards the incoming x-rays appear dark, while moments opposing the x-ray direction appear bright (see Suppl. Fig. 2(c-d). For each x-ray polarization, an exposure time of two seconds is chosen, while switching polarizations regularly takes one second. This gives an overall time of roughly three seconds ($\tau_m \approx 3\,\text{seconds}$) to obtain an XMCD image.

Initially, we find the thickness of $Ni_{80}Fe_{20}$ patterned on Pt where moment reorientations take place on the timescale of the acquisition time of the PEEM, see bottom panel of Suppl. Fig. 2(c). For this purpose, the sample is saturated along the x-ray direction, and subsequently, the thickness along the x-direction is found where switched magnetization appears as dark spots in an otherwise remanent state (all white). An XMCD sequence is taken to determine the reorientation rate, where 10 switches per image series is taken as the array with T_B at room temperature (296 K). As a check, the array of $Ni_{80}Fe_{20}$ nanomagnets on Si is imaged throughout and is still found to be in the magnetized state after 12 hours, see top panel of Suppl. Fig. 2(c). The sample is then heated in-situ up to 500 K, where the reorientation rate of the nanomagnets on Si is similar to the reorientation rate at room temperature for $Ni_{80}Fe_{20}$ on Pt, see top panel Suppl. Fig. 2(d). For the array with $Ni_{80}Fe_{20}$ nanomagnets on both Si and Pt (middle panel), it can be clearly seen that the reorientation rate on Si is significantly lower than that on Pt that, on average, results in a gray contrast. Hence, the energy barriers for nanomagnets on Pt are significantly lower than for those on Si for identical magnetic moments.

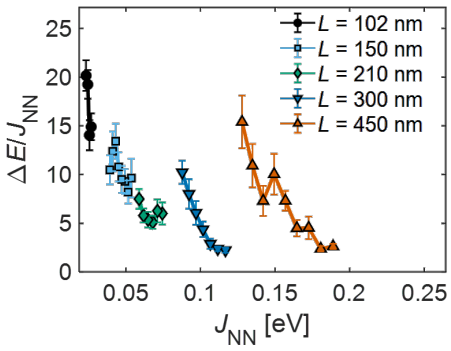

Suppl. Fig. 3. Point-dipolar energy of the magnetic configurations of kagome structures compared to the ground state energy normalized to the dipolar pre-factor ($\Delta E/J_{NN} = \langle E_{config} - E_{GS}\rangle/J_{NN}$) determined from X-PEEM images where each point corresponds to an average of 20 seven-ring structures for various combinations of L and h. Each colour series corresponds to a particular L and is plotted against J_{NN}, the dipolar pre-factor given by Eqn. (1). The error bars indicate the standard deviation. The lower value of J_{NN} for thinner nanomagnets results in poorer ordering, i.e. lower $\Delta E/J_{NN}$. Thus each line for a given L shows a downward trend from left (thin nanomagnets) to right (thicker nanomagnets).

VI REDUCED DIPOLAR ENERGY OF SEVEN-RING STRUCTURES

In order to compare the ordering between different seven-ring artificial kagome structures, we considered the reduced dipolar energy $\Delta E/J_{NN}$, using only the spin configuration $\hat{S}$ and their distance $\hat{r}$ in fractions of the lattice parameter in the dipolar configuration energy (Eqn. 19 for the dipolar energy). The reduced dipolar energy is calculated by dividing out the dipolar pre-factor J_{NN}, that contains all the geometrical information. The energy of each seven-ring structure is computed by summing the dipolar energy over all neighbours giving E_{config}, similar to the method used by Farhan *et al.* [14], and is repeated for all 20 seven-ring structures found in a single field-of-view PEEM XMCD image. The reduced dipolar energy of the ground-state configuration E_{GS} is computed with the two possible degenerate ground-state configurations given in Fig. 3(c) of the manuscript. The obtained $\Delta E/J_{NN}$ is the average excitation above the ground-state $\langle E_{config} - E_{GS}\rangle$ and the error is given by the standard deviation of the mean. Furthermore, $\Delta E/J_{NN}$ can be compared for various dipolar pre-factors (Suppl. Fig. 3), from which we conclude that, for each L, the increased coupling (higher J_{NN} due to increased thickness) results in better magnetic ordering.

VII ORDERING AND BLOCKING TEMPERATURE IN SEVEN-RING KAGOME STRUCTURES

In order to compare the magnetic ordering of kagome structures with differently sized nanomagnets, we plot the average configuration energies $\Delta E/J_{NN}$ with an experimentally determined blocking temperature $T_B(L,h)$ at two temperatures of 50 K and 86 K indicated by the dashed red lines in Suppl. Fig. 4(a,c). We have defined T_B as the temperature below which only 3 to 5 moment fluctuations were observed within 50 sec, corresponding to the time of 10 consecutive XMCD images. To determine the blocking temperature T_B as a function of L and h, we identified using X-PEEM the thickness h of kagome structures with $L = 450$ nm, 300 nm, 210 nm, 150 nm and 100 nm, for which $T = 50$ K and at $T = 86$ K are the blocking temperatures.

Since $T_B \propto h$, we can linearly interpolate the blocking temperatures for all remaining thicknesses, as given in Suppl. Fig. 4(b). The resulting average configuration energies $\Delta E(L, T_B)$ are plotted in Suppl. Fig. 4(c) for different nanomagnet lengths L and blocking temperatures $T_B(L,h)$. In Suppl. Fig. 4(c), we have included the location at each lateral dimension where an optimum magnetic ordering is obtained, i.e. a low value of $\Delta E(L, T_B)$. From the dashed black line through these low values of $\Delta E(L, T_B)$ it can be seen that larger lateral dimensions result in better magnetic ordering, with $\Delta E/J_{NN}$ closer to that of the ground state.

VIII MONTE CARLO SIMULATIONS

We used Monte Carlo (MC) simulations to compute the equilibrium configurations by modelling the individual nanomagnets as point-dipole macrospins and with Ising degrees of freedom along the length of each nanomagnet, arranged on a finite kagome lattice [1, 2, 15, 16]. The

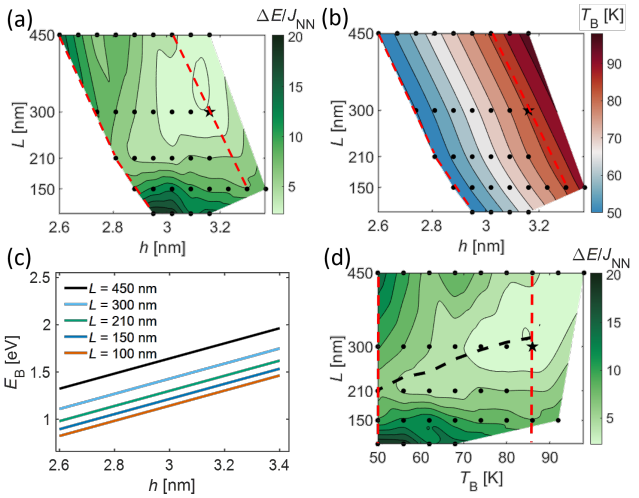

Suppl. Fig. 4. (a) The point-dipolar energy of magnetic configurations compared to the ground state normalized to the dipolar pre-factor ($\Delta E/J_{\mathrm{NN}} = \langle E_{\mathrm{config}} - E_{\mathrm{GS}}\rangle/J_{\mathrm{NN}}$). These values are determined from X-PEEM images where each point corresponds to nanomagnets with a particular L and h. Each data point corresponds to the average of $\Delta E/J_{\mathrm{NN}}$ for 20 seven-ring structures. The location of the observed global minimum in ΔE is indicated with a black star. (b) The experimentally obtained blocking temperatures $T_{\mathrm{B}}(L,h)$ at two temperatures of 50 K and 86 K (red dashed lines) with the remaining $T_{\mathrm{B}}(L,h) \propto h$ linearly interpolated at each L. The two blocking temperatures are also indicated with red dashed lines in (a) and (d). (c) Energy barrier simulations of nanomagnets for various L and h, with the resulting linear relationship between E_{B} and h. (d) The reduced configuration energy $\Delta E/J_{\mathrm{NN}}$ as a function of the interpolated blocking temperatures. Indicated with a dashed black line is the average minimum energy configuration at each blocking temperature, with a trend towards larger L and $T_{\mathrm{B}}(L,h)$ resulting in better magnetic ordering.

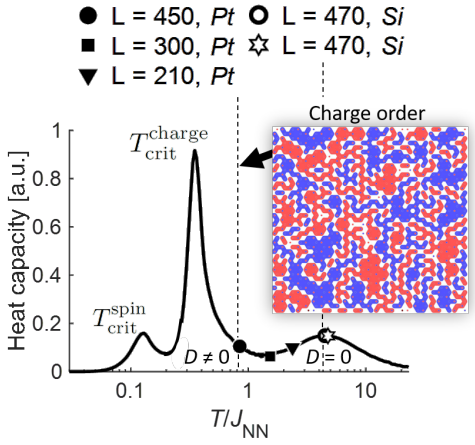

Suppl. Fig. 5. The heat capacity from MC simulations, showing three peaks corresponding to the paramagnetic-ice cross-over, and the two phase transitions $T_{\mathrm{crit}}^{\mathrm{charge}}$ and $T_{\mathrm{crit}}^{\mathrm{spin}}$, to the charge and spin-ordered phases, respectively. The filled markers correspond to the reduced temperatures determined from the X-PEEM images for an artificial kagome spin ice with interfacial DMI. The open markers correspond to the reduced temperatures obtained experimentally for systems without the interfacial DMI, with the open circle corresponding to the values from Farhan *et al.* [17]. The dashed lines indicate two systems with and without DMI (D), and similar J_{NN}. The extent of the twofold degenerate charge-ordered domains obtained from X-PEEM images is indicated in red and blue in the inset for $L = 450$ nm on Pt with $T/J_{\mathrm{NN}} = 0.84$.

Hamiltonian is as follows:

$$H = \frac{1}{2}\sum_{<i,j>} \frac{J_{\mathrm{NN}}}{(r_{ij}/a)^3}\left[\hat{\mathbf{S}}_i \cdot \hat{\mathbf{S}}_j - 3\left(\hat{\mathbf{S}}_i \cdot \hat{\mathbf{r}}_{ij}\right)\left(\hat{\mathbf{S}}_j \cdot \hat{\mathbf{r}}_{ij}\right)\right], \tag{19}$$

where $\hat{\mathbf{S}}_i$ is the macrospin unit vector for the macrospin i, $\hat{\mathbf{r}}_{ij}$ is the unit vector connecting the macrospins i and j, and r_{ij} is the distance between the neighbouring macrospins with, a, the neareast-neighbour distance. Interactions up to fifth nearest-neighbours ($r_{ij} = 3.55$) are required to obtain converging results. The simulations were carried out on an array containing $N = 2646$ macrospins with periodic boundary conditions. The simulations are performed with a dipolar pre-factor $J_{\mathrm{NN}} = 379$ K to which the temperatures are scaled.

We then perform the simulation in three regions with varying temperature stepsizes and MC sweeps. Here an MC sweep is defined as N single site MC steps followed by $N/2$ hexagonal loop MC steps, where the latter loop algorithm is the same as that used in Ref. [1]. The high-temperature paramagnetic to Spin Ice I crossover is simulated by varying the temperature from 9000 K down to 600 K in steps of 100 K with 10 000 MC sweeps at each temperature to obtain a well-converged heat capacity. The Spin Ice I to Spin Ice II transition ($T_{\mathrm{crit}}^{\mathrm{charge}}$) is simulated by varying the temperature from 600 K down to 100 K in steps of 5 K and with 10 000 MC sweeps. The Spin Ice II to Long-Range Order transition ($T_{\mathrm{crit}}^{\mathrm{spin}}$) is simulated by varying the temperature from 100 K down to 1 K in steps of 1 K with 100 000 MC sweeps, eventually resulting in a system-spanning long-range ordered kagome spin ice. The resulting temperature-dependent heat capacity is given in Suppl. Fig. 5. Furthermore, the reduced temperatures (dashed lines) of the experimental systems with and without DMI are indicated. For $L = 450$ nm on Pt (with DMI) it is found that $T/J_{\mathrm{NN}} = 0.84$ and for $L = 450$ nm on Si (without DMI) the reduced temperature $T/J_{\mathrm{NN}} = 4.49$. Hence, the obtained reduced temperature of the nanomagnets with DMI is closer to the charge-order phase transition.

IX REFERENCES

[1] G. Mller and R. Moessner, Phys. Rev. B **80**, 140409 (2009).

[2] G.-W. Chern, P. Mellado, and O. Tchernyshyov, Phys. Rev. Lett. **106**, 207202 (2011).

[3] M. Cubukcu, J. Sampaio, K. Bouzehouane, D. Apalkov, A. V. Khvalkovskiy, V. Cros, and N. Reyren, Phys. Rev. B **93**, 020401 (2016).

[4] H. T. Nembach, J. M. Shaw, M. Weiler, E. Ju, and T. J. Silva, Nature Physics **11**, 825 (2015).

[5] S. Y. Liashko, H. Jnsson, and V. M. Uzdin, New J. Phys. **19**, 113008 (2017).

[6] W. E, W. Ren, and E. Vanden-Eijnden, The Journal of Chemical Physics **126**, 164103 (2007).

[7] C. Abert, Eur. Phys. J. B **92**, 120 (2019).

[8] S. Koraltan, M. Pancaldi, N. Leo, C. Abert, C. Vogler, K. Hofhuis, F. Slanovc, F. Bruckner, P. Heistracher, M. Menniti, P. Vavassori, and D. Suess, Phys. Rev. B **102**, 064410 (2020).

[9] C. Abert, L. Exl, F. Bruckner, A. Drews, and D. Suess, Journal of Magnetism and Magnetic Materials **345**, 29 (2013).

[10] C. Geuzaine and J.-F. Remacle, International Journal for Numerical Methods in Engineering **79**, 1309 (2009).

[11] See Supplemental Material at [URL will be inserted by publisher] for [Supplementary Information document].

[12] L. Le Guyader, A. Kleibert, A. Fraile Rodrguez, S. El Moussaoui, A. Balan, M. Buzzi, J. Raabe, and F. Nolting, Journal of Electron Spectroscopy and Related Phenomena Photoelectron microscopy, Time resolved pump-probe PES, **185**, 371 (2012).

[13] J. Sthr, Y. Wu, B. D. Hermsmeier, M. G. Samant, G. R. Harp, S. Koranda, D. Dunham, and B. P. Tonner, Science **259**, 658 (1993).

[14] A. Farhan, A. Kleibert, P. M. Derlet, L. Anghinolfi, A. Balan, R. V. Chopdekar, M. Wyss, S. Gliga, F. Nolting, and L. J. Heyderman, Phys. Rev. B **89**, 214405 (2014).

[15] I. A. Chioar, B. Canals, D. Lacour, M. Hehn, B. Santos Burgos, T. O. Mente, A. Locatelli, F. Montaigne, and N. Rougemaille, Phys. Rev. B **90**, 220407 (2014).

[16] B. Canals, I.-A. Chioar, V.-D. Nguyen, M. Hehn, D. Lacour, F. Montaigne, A. Locatelli, T. O. Mente, B. S. Burgos, and N. Rougemaille, Nature Communications **7**, 11446 (2016).

[17] A. Farhan, P. M. Derlet, L. Anghinolfi, A. Kleibert, and L. J. Heyderman, Phys. Rev. B **96**, 064409 (2017).